The Astrophysical Journal, 963:139 (15pp), 2024 March 10 https://doi.org/10.3847/1538-4357/ad2079

2.5D Magnetohydrodynamic Simulation of the Formation and Evolution of Plasmoids in Coronal Current Sheets

Sripan Mondal[1], Abhishek K. Srivastava[1,6], David I. Pontin[2], Ding Yuan[3,4], and Eric R. Priest[5]
[1] Department of Physics, Indian Institute of Technology (BHU), Varanasi 221005, India; asrivastava.app@iitbhu.ac.in
[2] School of Information and Physical Sciences, University of Newcastle, Australia
[3] Shenzhen Key Laboratory of Numerical Prediction for Space Storm, Institute of Space Science and Applied Technology, Harbin Institute of Technology, Shenzhen, Guangdong, People's Republic of China; yuanding@hit.edu.cn
[4] Key Laboratory of Solar Activity and Space Weather, National Space Science Center, Chinese Academy of Sciences, Beijing, People's Republic of China
[5] Mathematics Institute, St Andrews University, KY16 9SS, St Andrews, UK
Received 2023 October 11; revised 2024 January 9; accepted 2024 January 12; published 2024 March 7

Abstract

In the present paper, using MPI-AMRVAC, we perform a 2.5D numerical magnetohydrodynamic simulation of the dynamics and associated thermodynamical evolution of an initially force-free Harris current sheet subjected to an external velocity perturbation under the condition of uniform resistivity. The amplitude of the magnetic field is taken to be 10 G, typical of the solar corona. We impose a Gaussian velocity pulse across this current sheet that mimics the interaction of fast magnetoacoustic waves with a current sheet in the corona. This leads to a variety of dynamics and plasma processes in the current sheet, which is initially quasi-static. The initial pulse interacts with the current sheet and splits into a pair of counterpropagating wavefronts, which form a rarefied region that leads to an inflow and a thinning of the current sheet. The thinning results in Petschek-type magnetic reconnection followed by a tearing instability and plasmoid formation. The reconnection outflows containing outward-moving plasmoids have accelerated motions with velocities ranging from 105 to 303 km s^{-1}. The average temperature and density of the plasmoids are found to be 8 MK and twice the background density of the solar corona, respectively. These estimates of the velocity, temperature, and density of the plasmoids are similar to values reported from various solar coronal observations. Therefore, we infer that the external triggering of a quasi-static current sheet by a single-velocity pulse is capable of initiating magnetic reconnection and plasmoid formation in the absence of a localized enhancement of resistivity in the solar corona.

Unified Astronomy Thesaurus concepts: Solar atmosphere (1477); Solar corona (1483); Magnetohydrodynamics (1964); Magnetic fields (994); Solar magnetic reconnection (1504)

Supporting material: animations

1. Introduction

Reconnection is a fundamental physical process of magnetized plasma. It can convert stored magnetic energy into thermal energy, bulk fluid kinetic energy, and charged particle energy at astronomical, solar system, and laboratory scales. (See the review articles by Biskamp et al. 2000; Birn & Priest 2007; Zweibel & Yamada 2009; Uzdensky 2011; Treumann & Baumjohann 2015; Loureiro & Uzdensky 2016; Yamada et al. 2016; Pontin & Priest 2022, and references cited therein for details.) Magnetic reconnection takes place when magnetic fields of differing orientations are brought together in close proximity, with a rapid rotation of the magnetic vector across a thin layer of high electric current density termed as a current sheet (CS; Cowling 1953; Priest & Forbes 1986; Priest 2014; Pontin & Priest 2022). Due to the presence of high-resolution observatories, the large cohort of observational signatures of magnetic reconnection such as bidirectional flows, heating, and associated plasma dynamics are ubiquitously seen in the solar corona. However, the detailed nature of CS formation and its evolution resulting in magnetic reconnection and solar eruptions are yet to be fully understood. Therefore, an important way to extract the detailed physics behind magnetic reconnection under various plasma conditions, such as those in the solar corona, is to simulate or model the formation and evolution of a CS numerically. To model the evolution of a CS and the resulting magnetic reconnection, either internal perturbations such as a local resistivity enhancement or external perturbations in the form of magnetohydrodynamic (MHD) waves are needed. The use of MHD waves to perturb the CS gives rise to externally driven or forced reconnection. The onset and features of different types of magnetic reconnection and the advances in modeling the reconnection scenario are discussed in various review articles cited above.

Consider a thin, elongated CS in the solar corona. When its aspect ratio (i.e., the ratio of the length to width of the CS) is sufficiently large ($\gtrsim$100), then beyond a critical value of the Lundquist number ($S_L = LV_A/\eta > 3 \times 10^4$) three distinct phases of nonlinear evolution of reconnection can be characterized (Bhattacharjee et al. 2009; Baty 2012). In the initial stage, the CS system evolves to a quasi-steady but transient state having Sweet–Parker-like characteristics with an extended, thin CS. After this stage, a rapid secondary instability sets in to produce plasmoids or magnetic islands along the fragmented CS. Lastly, the system evolves to a nonlinear phase in which it exhibits rapid and impulsive reconnection. In this third and final stage, some of the smaller islands coalesce to form larger islands that are eventually

[6] Corresponding author.

convected outwards through the CS. The formation of plasmoids results in a higher reconnection rate under coronal conditions than the one predicted by the Sweet–Parker model, but similar to the normalized reconnection rate obtained with the Petschek model, i.e., $\pi/[8 \ln S]$. Since the solar corona has a high value of S_L (typically 10^{12}–10^{14}), the growth of a plasmoid instability in an elongated CS is expected during the onset of solar flares. Therefore, plasmoid instabilities are considered as a viable mechanism to explain the high reconnection rate reported from the observations of flares. As a result, plasmoid instabilities have been studied extensively in the literature via numerical simulations (e.g., Bhattacharjee et al. 2009; Huang & Bhattacharjee 2010; Baty 2012; Huang & Bhattacharjee 2012, 2013; Huang et al. 2015; Huang & Bhattacharjee 2016). At the same time, the advent of high-resolution observational facilities has given rise to several observations of moving plasma blobs along an elongated CS. Also, jets and flows, which are the dynamical response of magnetic reconnection, have been observed. They have, therefore, confirmed observationally the formation and motion of the plasmoids found in simulations (e.g., Asai et al. 2001; Liu et al. 2009; Takasao et al. 2012; Zhang & Ji 2014; Zhang et al. 2016; Cheng et al. 2018; Chen et al. 2022; Yan et al. 2022). Longcope et al. (2018) inferred that superarcade downflows in an elongated CS may well be evidence of plasmoids. But later on, Shen et al. (2022) suggested that these dark downflows are basically self-organized structures generated during the interaction of reconnection outflows with the flare arcade.

In the dynamic solar corona, a CS can be easily perturbed by photospheric footpoint motions or MHD waves, potentially leading to magnetic reconnection. For example, a flare can be initiated by another distant flare via superthermal particle beams and shock waves propagating from the earlier flare site (Norman & Smith 1978; Svestka 1981; Fárník et al. 1983). Observations of this kind of sympathetic flare initiated by MHD waves or shock waves have also been reported in the literature (Wang et al. 2001; Ofman & Liu 2018; Zhou et al. 2020). A few numerical simulations have studied the external forcing of reconnection and tearing-mode instabilities by fast-mode MHD waves or shocks (Sakai & Washimi 1982; Sakai 1983; Odstrcil & Karlicky 1997b; Potter et al. 2019). However, all of these studies have implemented an anomalous resistivity to facilitate fast reconnection. Therefore the role of external forcing on the different stages of reconnection in the absence of a localized resistivity enhancement has not yet been studied in a comprehensive manner, which is what we are attempting here. Now both CSs and extreme-ultraviolet (EUV) waves are likely to be commonly present in the solar corona (e.g., Zheng et al. 2014; Chen 2017; Cheng et al. 2018; French et al. 2020). Therefore it is important to study this aspect of external forcing more carefully with specific initial physical conditions such as typical solar coronal CSs and fast external velocity disturbances.

In our present paper, we investigate the physical role of transient external velocity perturbations on the dynamics of an initially quasi-stable CS. We do not incorporate a localized enhancement of resistivity (as in Odstrcil & Karlicky 1997a; Potter et al. 2019). Rather, we adopt uniform resistivity throughout the simulation domain. Since the generation of transient velocity disturbances is likely to be impulsive rather than periodic in practice, we prescribe an initial, unidirectional velocity pulse rather than imposing periodic perturbations. The detailed physical scenario for the different phases of the dynamics of a coronal CS is investigated. The formation, evolution, and physical characteristics of the plasmoids are studied. We present the numerical setup of the model in Section 2 followed by results in Section 3. In Section 4, we summarize the results and discuss a few key points related to the physical feasibility of the dynamics. We compare with observations and consider the effect of the velocity amplitude of the disturbances on CS dynamics. In Section 5, we conclude our work, emphasizing its importance as a comprehensive study of externally driven reconnection under solar coronal conditions.

2. Numerical Setup of the Magnetohydrodynamic Model

Using the open source Message Passing Interface–Adaptive Mesh Refinement-Versatile Advection Code (MPI-AMRVAC;[7] Keppens et al. 2012; van der Holst et al. 2012; Porth et al. 2014; Xia et al. 2018), we construct a numerical model of the dynamics and reconnection process in a coronal CS. The spatial dimensions are −100 to 100 Mm in the x-direction and 0–200 Mm in the y-direction. We run the simulation for 1178 s (around 20 minutes). The spatial resolution before any refinement is 1.56 Mm in both the directions, which is then subjected to a maximum of four levels of adaptive mesh refinement. This results in a smallest cell of size 97.5 km. To examine the effect of an external velocity perturbation on the dynamics of a force-free Harris CS, we solve the following set of well known MHD equations numerically. We use a "two-step" method for temporal integration and the "Harten–Lax–van Leer" scheme to calculate the flux at cell interfaces

$$\frac{\partial \rho}{\partial t} + \nabla \cdot (\rho \boldsymbol{v}) = 0, \tag{1}$$

$$\frac{\partial}{\partial t}(\rho \boldsymbol{v}) + \nabla \cdot [\rho \boldsymbol{v}\boldsymbol{v} + (p + \boldsymbol{B}^2/2)\boldsymbol{I} - \boldsymbol{B}\boldsymbol{B}] = 0, \tag{2}$$

$$\frac{\partial e}{\partial t} + \nabla \cdot (e\boldsymbol{v} + (p + \boldsymbol{B}^2/2)\boldsymbol{v} - \boldsymbol{B}\boldsymbol{B} \cdot \boldsymbol{v}) = \eta \boldsymbol{J}^2 - \boldsymbol{B} \cdot \nabla \times (\eta \boldsymbol{J}), \tag{3}$$

$$\frac{\partial \boldsymbol{B}}{\partial t} + \nabla \cdot (\boldsymbol{v}\boldsymbol{B} - \boldsymbol{B}\boldsymbol{v}) + \nabla \times (\eta \boldsymbol{J}) = 0, \tag{4}$$

$$\nabla \cdot \boldsymbol{B} = 0, \tag{5}$$

$$\boldsymbol{J} = \nabla \times \boldsymbol{B}. \tag{6}$$

Here ρ, $\boldsymbol{B}$, $\boldsymbol{v}$, $\boldsymbol{J}$, and η are the mass density, magnetic field vector, velocity vector, current density vector, and resistivity, respectively. Initially, ρ and T are set to uniform values of 2.34×10^{-15} g cm^{-3} (ρ^*) and 1 MK (T^*), respectively, which are appropriate for the solar corona. Initially, the thermal pressure p is calculated to be 0.32 dyne cm^{-2} (P^*) using the ideal gas law. The factors used to normalize the length, magnetic field, velocity, and current density are $L^* = 10^9$ cm, $B^* = 2$ G, $V^* = 116.45$ km s^{-1}, and $J^* = 4.77$ statA cm^{-2}, respectively. e is the total energy density defined as

$$e = \frac{p}{\gamma - 1} + \frac{\rho v^2}{2} + \frac{B^2}{2}, \tag{7}$$

with $\gamma = \frac{5}{3}$ being the ratio of specific heats for a monatomic gas. Gravity is not included in our simulations as we are

[7] http://amrvac.org

modeling a localized segment of a coronal CS and we ignore stratification. Note that we use continuous boundary specifications for all the boundaries in which the variables are extrapolated using the closest inner mesh cell value to all of the ghost cells, i.e., the gradient is kept zero for all the variables. We choose the background parameters density, temperature, and magnetic field in such a way that our simulation and its corresponding outputs mimic the observations of reconnection in the Sun's corona with a plasma β of 0.079. Moreover, we discuss the detailed physics of reconnection that may trigger solar eruptions at coronal heights, which is important for interpreting the observations. In the energy equation, we have not included energy losses via thermal conduction or radiative cooling in our primary model. In addition, no background heating term has been added, but an ohmic heating term has been included for consistency with the resistive term in the magnetic induction equation (Equation (4)). The initial magnetic field is given by

$$B_x = 0, \tag{8}$$

$$B_y = -B_0 \tanh\left(\frac{x}{l}\right), \tag{9}$$

$$B_z = B_0 \,\mathrm{sech}\left(\frac{x}{l}\right), \tag{10}$$

where B_x and B_y are the magnetic field components in the plane of a force-free CS. B_z is the guide field essential for providing force balance to maintain the system in initial equilibrium in the absence of a plasma pressure gradient. The relevance of using a guide field is discussed in Appendix B. Basically, we use a similar initial magnetic field configuration to that described in Section 3.2.4 of Xia et al. (2018) but with different values of the physical parameters. We set the magnetic field amplitude (B_0) and CS half-width (l) to be 10 G and 1.5 Mm, respectively. We adopt a uniform resistivity with dimensionless value 2×10^{-4} (corresponding to a magnetic diffusivity of 2.4×10^{8} m^2 s^{-1} in physical units) throughout the simulation domain, which gives a Lundquist number of 4.8×10^{5}. This is reasonable for coronal applications since the limitations of current numerical simulations preclude much higher values. Sen & Keppens (2022) used a similar dimensionless resistivity in their numerical simulation of coronal reconnection. It is also similar to those used in the study of plasmoid instabilities by various authors (e.g., Bhattacharjee et al. 2009; Huang & Bhattacharjee 2010, 2012, 2013, 2016; Huang et al. 2015; Sen & Keppens 2022).

To disturb the CS which is initially in quasi-static equilibrium, we impose an external velocity perturbation in the x-direction in the form of a Gaussian pulse given by

$$v_x = v_0 \exp\left(-\frac{(x - x_0)^2 + (y - y_0)^2}{w^2}\right). \tag{11}$$

Here x_0 is set at 15 Mm away from the center of the CS at $x = 0$ and y_0 is set at a height of 100 Mm in the middle of the domain in order to minimize the finite boundary effects. The width of this Gaussian pulse (w) is taken to be 4 Mm. The amplitude (v_0) of the velocity pulse is 350 km s^{-1}, which is $0.6v_A$, where $v_A = 580$ km s^{-1} is the Alfvén speed for our choice of parameters. This transient velocity pulse differs from the periodic disturbance used in Potter et al. (2019). Solar eruptions are accompanied by the generation and propagation of EUV waves away from the eruption site in a transient manner (e.g., Zheng et al. 2014; Cheng et al. 2018; Li et al. 2018; Zheng et al. 2018, 2022). They may sometimes in turn trigger reconnection, oscillations, eruptions, and resonant energy transfer in other regions, especially where prominences, coronal loops, or ambient localized coronal magnetic structures are located. In our model we mimic such a process by a Gaussian velocity pulse. Observational studies report the velocity of fast MHD waves or EUV waves to be of order 350 km s^{-1} or even higher. So for solar coronal conditions where the fast MHD wave speed is around 1000 km s^{-1}, the amplitude of the velocity pulse used in this work is appropriate. To explore the detailed physical behavior of reconnection driven by such fast-mode perturbations, we choose to impose (i) a straight local segment of the coronal CS without curvature; (ii) uniform coronal plasma conditions without structuring; and (iii) no energy loss or heating terms in the energy equation. These complexities will be included in future works.

3. Results

We start from a force-free vertically elongated CS in initial equilibrium. We first performed a test run (not shown in the paper) to examine whether the CS undergoes thinning and plasmoid formation in the absence of external perturbations or not. We find that due to the presence of the finite uniform resistivity in our simulation domain, the CS undergoes slow diffusion only. That is, no thinning and plasmoid formation occurs without the external velocity perturbation. We also tested whether the chosen value of the physical resistivity is higher than the numerical resistivity for the considered resolution. We find that we can safely consider the dynamics to be dependent on physical resistivity. The details of the comparison between physical and numerical resistivity are discussed in Appendix A in detail.

As we perturb the CS via a velocity pulse of 350 km s^{-1}, it undergoes temporal evolution in the form of thinning followed by fragmentation. This action further gives rise to the formation of plasmoids or magnetic islands. The left panel of Figure 2 shows the temporal evolution of the maximum value of the outflow velocity v_y along the CS. It shows that the outflow velocity increases with time in an unsteady manner and finally enters an impulsive phase indicative of a plasmoid instability. The middle panel of Figure 2 shows the temporal evolution of $\eta J_{\max}$, which we consider as a proxy of the reconnection rate, as often assumed (e.g.,Yokoyama & Shibata 1997; Baty 2012). It also shows unsteady behavior as the impulsive bursty phase is approached. We discuss each of the phases of the dynamics of the CS along with their characteristics as follows.

3.1. Different Phases of the Dynamics of the Current Sheet

3.1.1. Thinning of the Current Sheet

As the velocity pulse crosses the CS, it splits into two counterpropagating wavefronts from the CS toward the lateral boundaries. The reflected one traverses to the left of the CS while the transmitted one traverses to the right. These counterpropagating wavefronts produce a fast-mode expansion

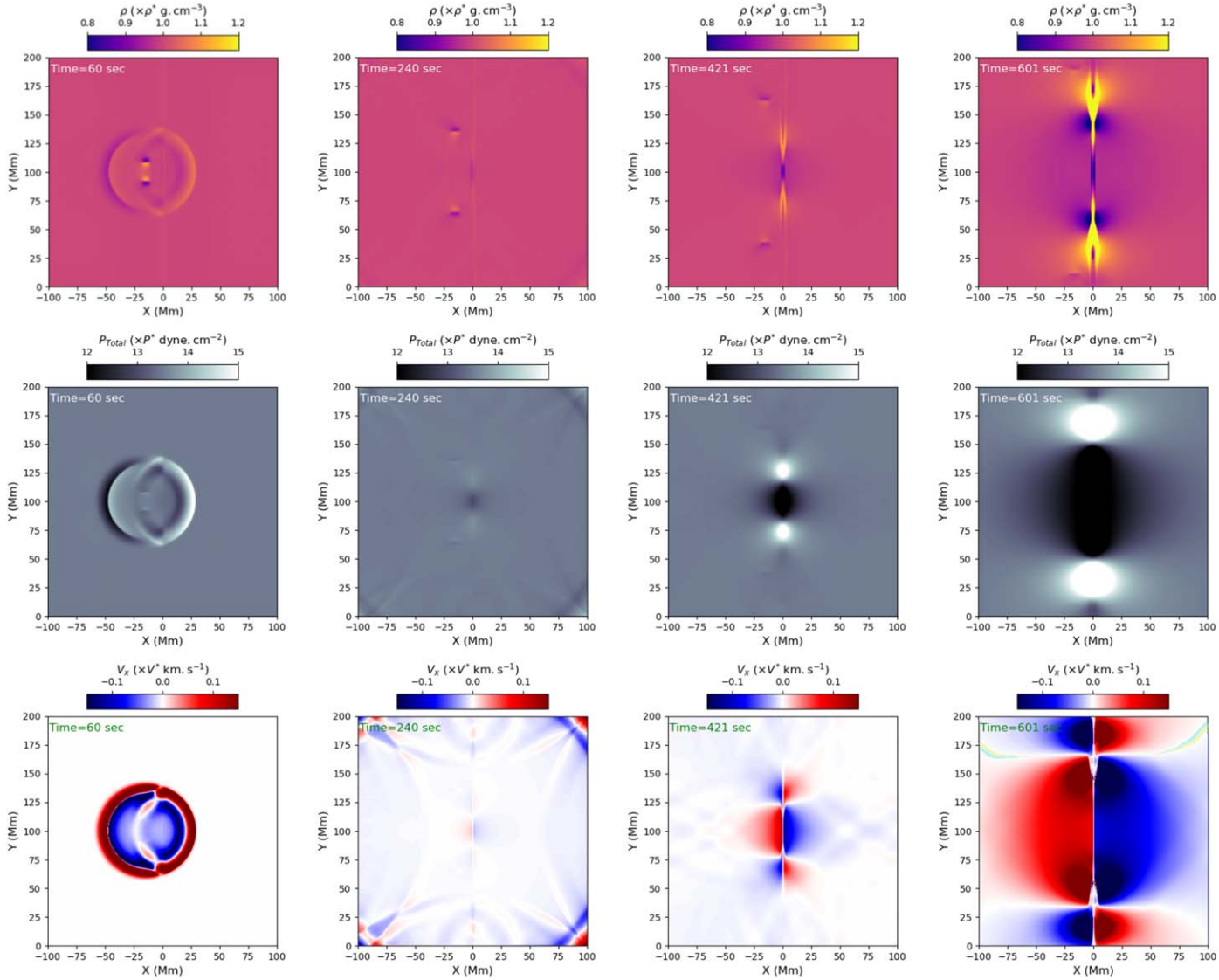

Figure 1. Snapshots of various quantities at times 60, 240, 421, and 601 s are shown from left to right. Top: the density distribution maps. A slow-mode shock propagates along the magnetic field lines parallel to the CS and causes the density in the middle of the CS to decrease. Middle: the total pressure distribution (kinetic + magnetic) maps. At 240 s, the total pressure in the CS region has become smaller than in its surroundings. As time progresses, this total pressure gradient increases. Bottom: the x-component of the velocity maps. The inward total pressure gradient and density gradient toward the CS causes an inflow toward the CS which drives magnetic reconnection. The evolution of these quantities from the start of the simulation to 601 s is available as an animation. The real-time animation duration is 5 s. The start of the thinning phase, bidirectional outflows, and fragmentation of the CS are annotated in the animation of the density map.

(An animation of this figure is available.)

which results in a decrease of density in the CS region (as shown in the top row of Figure 1). Similarly, an inward total pressure gradient is established toward the CS from its immediate surroundings (as shown in the middle row of Figure 1). These inward gradients of density and total pressure lead to an inflow toward the CS from the surrounding region (as shown in the bottom panel of Figure 1), resulting in gradual thinning of the CS with time. These entire dynamics are even better seen in the animations accompanying Figure 1. We now examine the detailed characteristics of this thinning phase.

To quantify the change in CS configuration during this unsteady phase, we take the CS width, CS length, and ratio of length to width as the important factors. To estimate the CS width and length, we take a horizontal slit across the CS at $y = 100$ Mm and a vertical slit along the CS at $x = 0$ Mm, respectively. We discover that the current density distributions across as well as along the CS have maxima at $x = 0$ Mm and $y = 100$ Mm, respectively, and we fit them with Gaussian functions given by

$$G(s, \sigma) = C \exp\left(\frac{-(s - \bar{S})^2}{2\sigma^2}\right). \quad (12)$$

The obtained value of σ is then used to calculate the FWHM of the distribution as

$$\mathrm{FWHM} = 2\sqrt{2\,\sigma^2}\ln 2. \quad (13)$$

These FWHMs are taken as estimates of the CS width and CS length. We find that, during this unsteady phase of reconnection, the CS undergoes a gradual thinning dynamically, as shown in the temporal profile of CS width, which is presented as a red curve in the right panel of Figure 2. The rate of

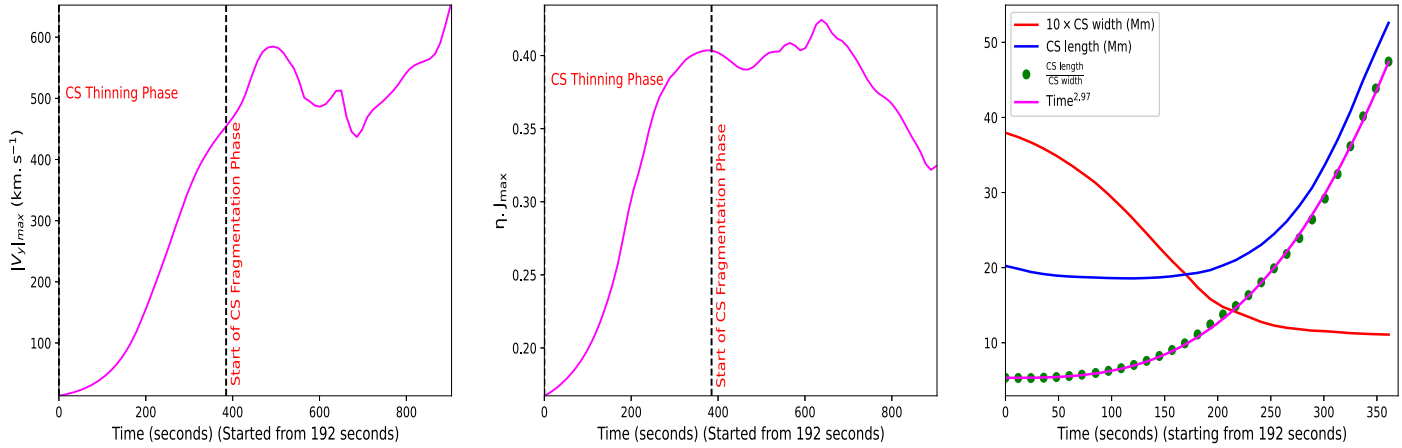

Figure 2. Left: the temporal evolution of the maximum of the outflow velocity v_y along the CS, which shows a gradual increase followed by an impulsive bursty part due to the plasmoid instability. Middle: the temporal evolution of $\eta J_{\rm Max}$ along the CS, which is an another proxy of the reconnection rate. Right: temporal evolution of the CS width at a height of 100 Mm, CS length and the aspect ratio of the CS, i.e., the ratio of its length to width. The temporal evolution of the aspect ratio of the CS follows a power law with exponent 2.97.

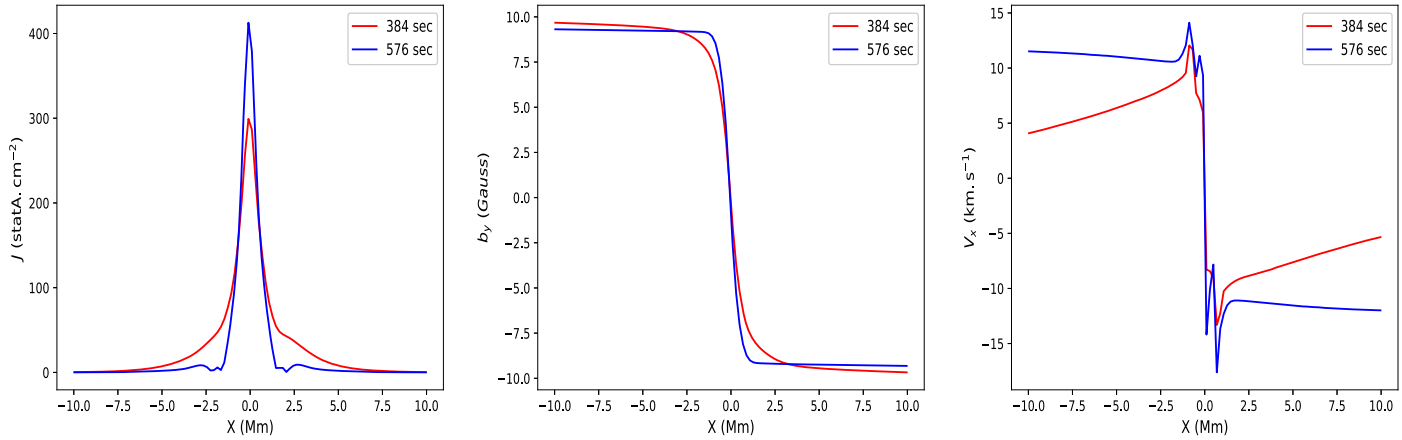

Figure 3. The distribution of total current density (J), magnetic field along the CS (b_y), and inflow velocity (v_x; from left to right) across the CS at $y = 100$ Mm. The gradual decrease of b_y, and increase of J and v_x toward the CS from the surroundings at 384 s, just at the beginning of the bidirectional outflows, are signatures of Petschek-type reconnection. Also, the steepness of the gradients of these quantities at 576 s just before the fragmentation starts, are a signature of Sweet–Parker reconnection.

thinning increases with time, resulting in an unsteady characteristic of the thinning process. The right panel of Figure 2 also shows the temporal evolution of the CS length (blue curve). It is evident that the measured CS length is not increasing significantly at the beginning of the thinning phase. But during the later phase, it starts to increase rapidly. Nevertheless the most important estimate for characterizing the time-dependent behavior of a dynamic CS is its aspect ratio. As shown in the right panel of Figure 2, the aspect ratio of the CS increases following a $t^{2.97}$ profile.

Now it is interesting to determine whether the reconnection during this thinning phase has Sweet–Parker or Petschek characteristics. Since the CS is dynamic, we check the character of the diffusion region to determine whether it is of Petschek type or Sweet–Parker type at the beginning of the bidirectional outflows and at the beginning of the fragmentation of the CS. Baty (2012) suggested that for the classical Petschek nature of reconnection to exist, there must be a gradual increase of the inflow velocity v_x as we move toward the CS from the inflow boundaries. Also, the inflow magnetic field b_y and the current density (J) should undergo a gradual decrease and increase, respectively, as we move toward the CS from the inflow domain boundaries for the reconnection to be Petscheck type. Now, in Figure 3, we find that all these three quantities possess the required signature of Petschek-like reconnection (red curves) at time 384 s at the beginning of the bidirectional outflows. But just before the start of CS fragmentation, the profiles of these quantities are more likely to be of Sweet–Parker nature as they show steep gradients across the CS. Therefore, we infer that during the unsteady transition phase before the fragmentation of the CS, the reconnection starts with a Petschek-like nature in a small diffusion region. As time progresses, the length of the diffusion region increases and finally becomes sufficiently elongated (with the aspect ratio attaining a value of 48) that it reaches a Sweet–Parker regime.

To support the Petschek-type reconnection scenario, we also look for signatures of the slow-mode shocks found in that model. Following Yokoyama & Shibata (1997), we extract the profiles of plasma density, plasma pressure, magnetic field, and current density across the CS just outside the diffusion layer. We take horizontal cuts at y = 125 Mm at time 384 s at the beginning of the bidirectional outflows. As shown in the left column of Figure 4, there are steep gradients in all the aforementioned physical parameters. The increase in density and kinetic pressure and decrease in magnetic field strength in

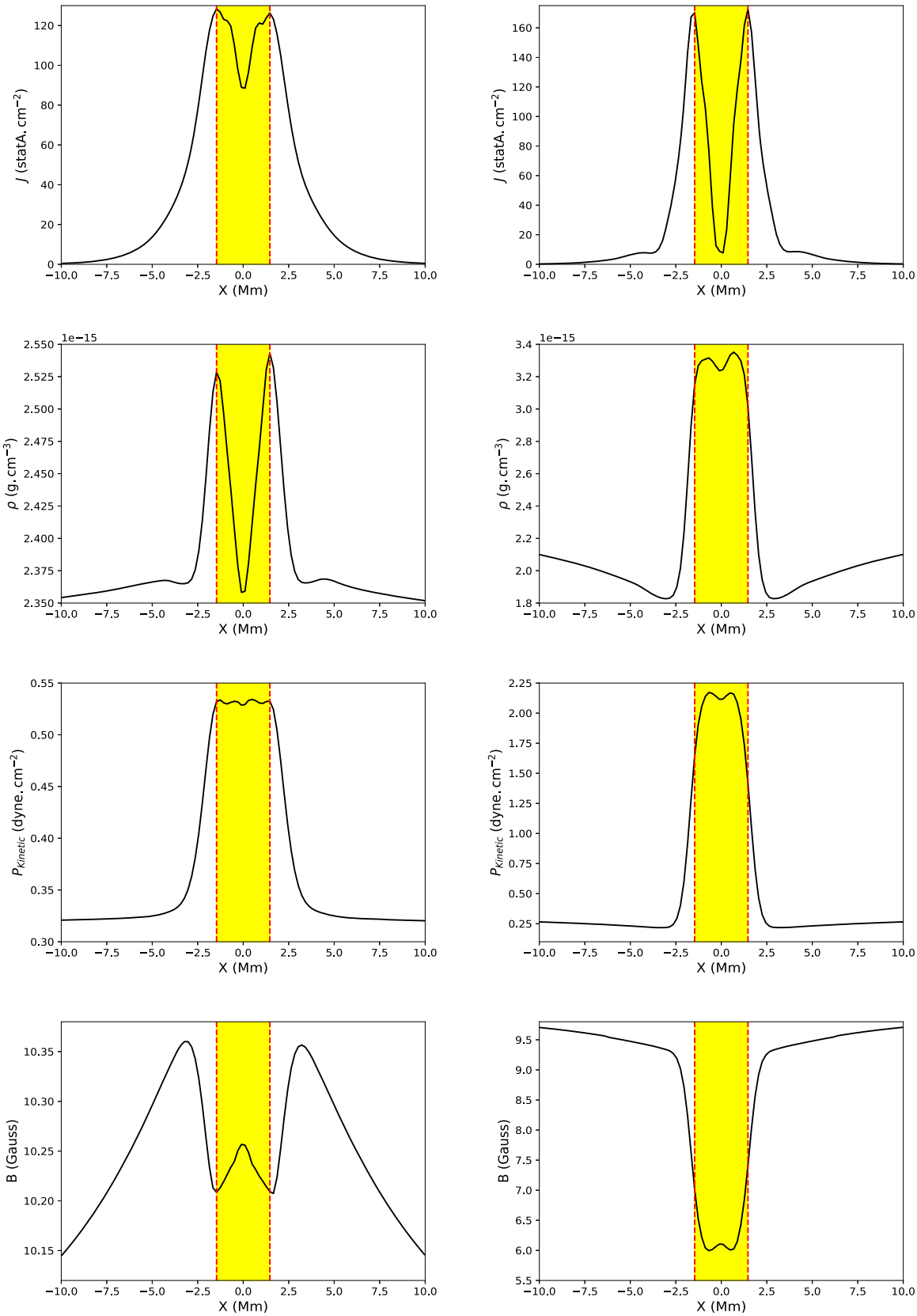

Figure 4. Profiles of the current density, plasma density, plasma pressure, and magnetic field across the CS. Left column: at $y = 125$ Mm and at time 384 s. Right column: at $y = 140$ Mm and at time 576 s just before the start of fragmentation of the CS. All the quantities possess steep gradients that are the signature of slow-mode MHD shocks. The maximum of the current density gives the approximate location of the shock, which is denoted by the red dashed vertical lines in the plots. The yellow shaded region is the outflow region.

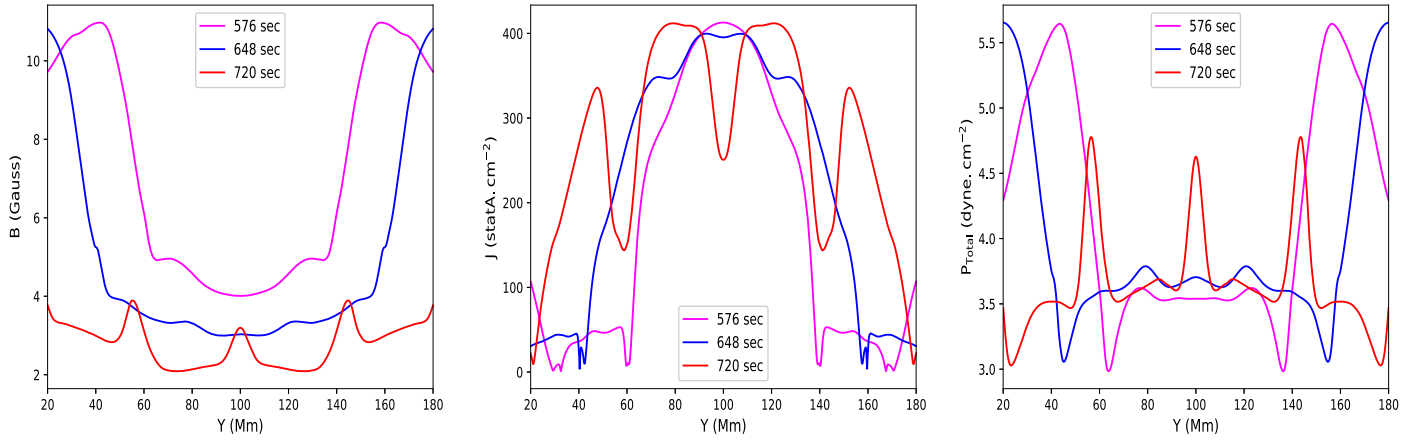

Figure 5. Profiles of various quantities along the CS at three times during its fragmentation. Left: total magnetic field (B). As time progresses, the region with a low magnetic field becomes stretched along the length of the CS while the value of magnetic field decreases. But the flattened profile of B also becomes fragmented and eventually three peaks of B appear, demonstrating the location of plasmoid formation. Middle: total current density (J). Low-J regions are those where plasmoids or magnetic islands have formed. Right: total pressure (kinetic + magnetic). High-pressure regions are formed during the fragmentation of the CS, and the low-pressure region in the middle of the CS indicates a region of plasmoid formation.

the vicinity of the layer, denoted by red dashed vertical lines, are all evidence of a slow-mode MHD shock at that height. Our estimated profiles are similar to those in Yokoyama & Shibata (1997). So the presence of shocks further confirms that the reconnection at the beginning of the bidirectional outflows is of Petschek type. As the CS evolves with time, however, the length of the diffusion layer increases and finally attains that of a Sweet–Parker CS. As previous literature (e.g., Priest & Forbes 1986; Baty 2012) suggested, even though the diffusion layer becomes Sweet–Parker type in the middle portion of the entire CS, there are signatures of comparatively shorter slow-mode shocks at the ends of the extended diffusion layers. So we repeat our estimate of the transverse profiles of the physical parameters at a height of $y = 140$ Mm at time 576 s during the beginning of the fragmentation of the diffusion layer at the middle of the CS. We find steep gradients and, more specifically, an increase in density and kinetic pressure and a decrease in magnetic field across the layer going into the outflow region, as before (shown in the right column of Figure 4). In addition, we notice that the substructuring of the plasma density, pressure, and magnetic field in the shocked region become less prominent at later times, which may signify a relative weakening of the slow-mode MHD shocks. However, the current density shows the opposite behavior, i.e., it becomes more substructured at later times.

3.1.2. Fragmentation of the Current Sheet

Once the CS is long enough that the ratio of the length to width of the CS reaches around 48 at time 576 s—compared to a value of 5 at the beginning of the thinning of the CS—it starts to fragment into small portions due to the onset of the tearing-mode instability (Furth 1963). This fragmentation is evident from small-scale substructuring of the profile of the total magnetic field magnitude along the CS, as shown in the left panel of Figure 5. Similarly, as shown in the middle panel of Figure 5, the profile of the total current density (J) starts to form a dip at a height of 100 Mm at time 576 s. As time progresses, the profile gets more flattened and the dips in J become even more prominent than earlier. Finally at 720 s, just before the visibility of the plasmoids in the mosaics in Figure 6, the dips are clearly showing fragmentation of current density along the CS (as shown in the middle panel of Figure 5). Likewise, in the right panel of Figure 5, it is evident that the sum of the kinetic and magnetic pressures has peaks corresponding to the dips in the current density profile. So the profile of the total pressure is also showing the signature of fragmentation of the elongated CS into smaller-length segments. This fragmentation has been further followed by formation of plasmoids at the dips of the current density or peaks of the total pressure and total magnetic field. The dips of current density at about 60 and 140 Mm are more than that at 100 Mm (as shown in the middle panel of Figure 5) during the onset of the primary stage of plasmoid formation.

Now let us determine whether the dips or peaks in Figure 5 are consistent with the allowable range of wavelength for the tearing-mode instability. We note that by this time the velocity disturbance has already passed out of the simulation zone, since there is no prominent reflection of the primary pulse from the boundary. The allowable range of wavelength for the tearing-mode instability (Furth 1963; Priest 2014) is

$$2\pi l < \lambda < 2\pi l\,(\mathrm{R}_m)^{\frac{1}{4}}, \tag{14}$$

where R_m is the magnetic Reynolds number defined as

$$\mathrm{R}_m = \frac{l v_{\mathrm{A}}}{\eta}, \tag{15}$$

with l being the half-width of the CS and η being the magnetic diffusivity. We calculate the average Alfvén speed and CS width between $y = 20$ Mm and $y = 180$ Mm at a time 720 s just before the plasmoids become visible. The average l and v_{A} are equal to 0.84 Mm and 528 km s^{-1}, respectively. This gives us a limit for the allowable wavelength for the tearing mode as 5.3 Mm $< \lambda <$ 34.7 Mm from Equation (14). Now in our case, the distance between the peaks or dips shown in the Alfvén speed in Figure 5 at 720 s is about 41 Mm. The slight difference in the estimated values may be due to the superposed reconnection outflows, which increase the distance between successive plasmoids. Thus, the distance between plasmoids is consistent with the theoretical estimate from the tearing-mode instability.

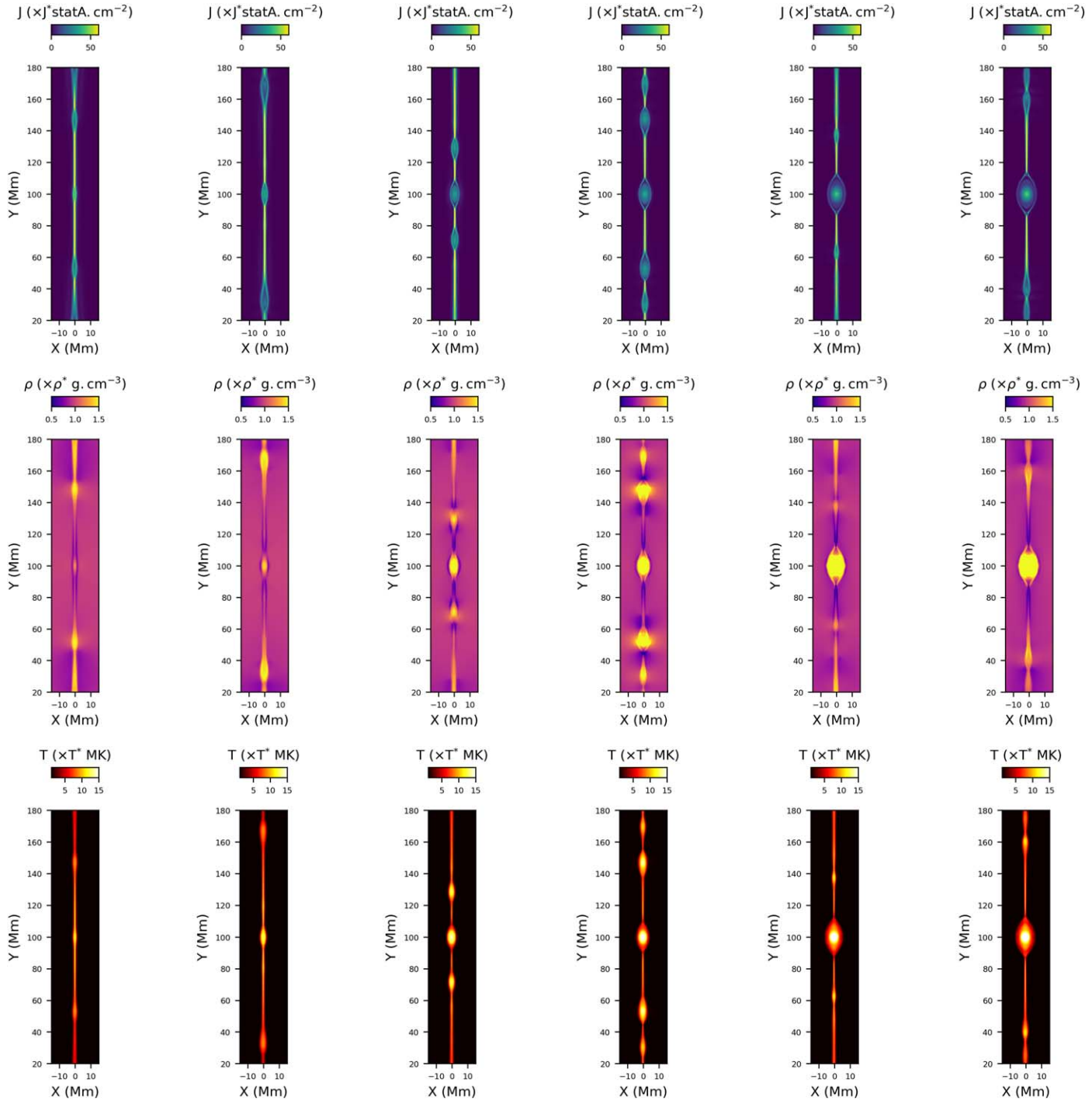

Figure 6. Top: snapshots of the total current density (J) at times 733, 781, 866, 938, 1130, and 1178 s, showing three stages of tearing of the CS and plasmoid formation and their outward movements along the CS along with the growth of a steady plasmoid at height of 100 Mm. Middle: similar snapshots of the density at the same times. Bottom: similar snapshots of the temperature at the same times. The entire evolution of the density and temperature from 613 to 1178 s and J from start of the simulation to 1178 s are available as an animation. The real-time animation duration is 10 s and only the two bottom portions of the animation play synchronously in time. The rectangular boxes (cyan for density and temperature; orange for J) are used in the animated versions to denote the field of view exhibited in this figure. The arrows and annotations in the animation of the density maps show the outward movements of the plasmoids formed in multiple stages of tearing.

(An animation of this figure is available.)

3.1.3. Multiple Stages of Plasmoid Instability in the Current Sheet

At the primary stage of tearing, three plasmoids become visible around 733 s. The plasmoids formed at 60 and 140 Mm are seen to move outward along the CS (as shown in first two columns of each row of Figure 6). On the other hand, the plasmoid formed at 100 Mm (middle of the CS) remains fixed due to the assumed symmetry of the magnetic configuration as well as the external velocity perturbation. This is discussed in detail in Appendix C. Nevertheless due to the outward movement of the plasmoids in the first stage, there is a loss of mass from the CS, and so a tendency for further thinning of the CS, which results in secondary tearing around 866 s. This

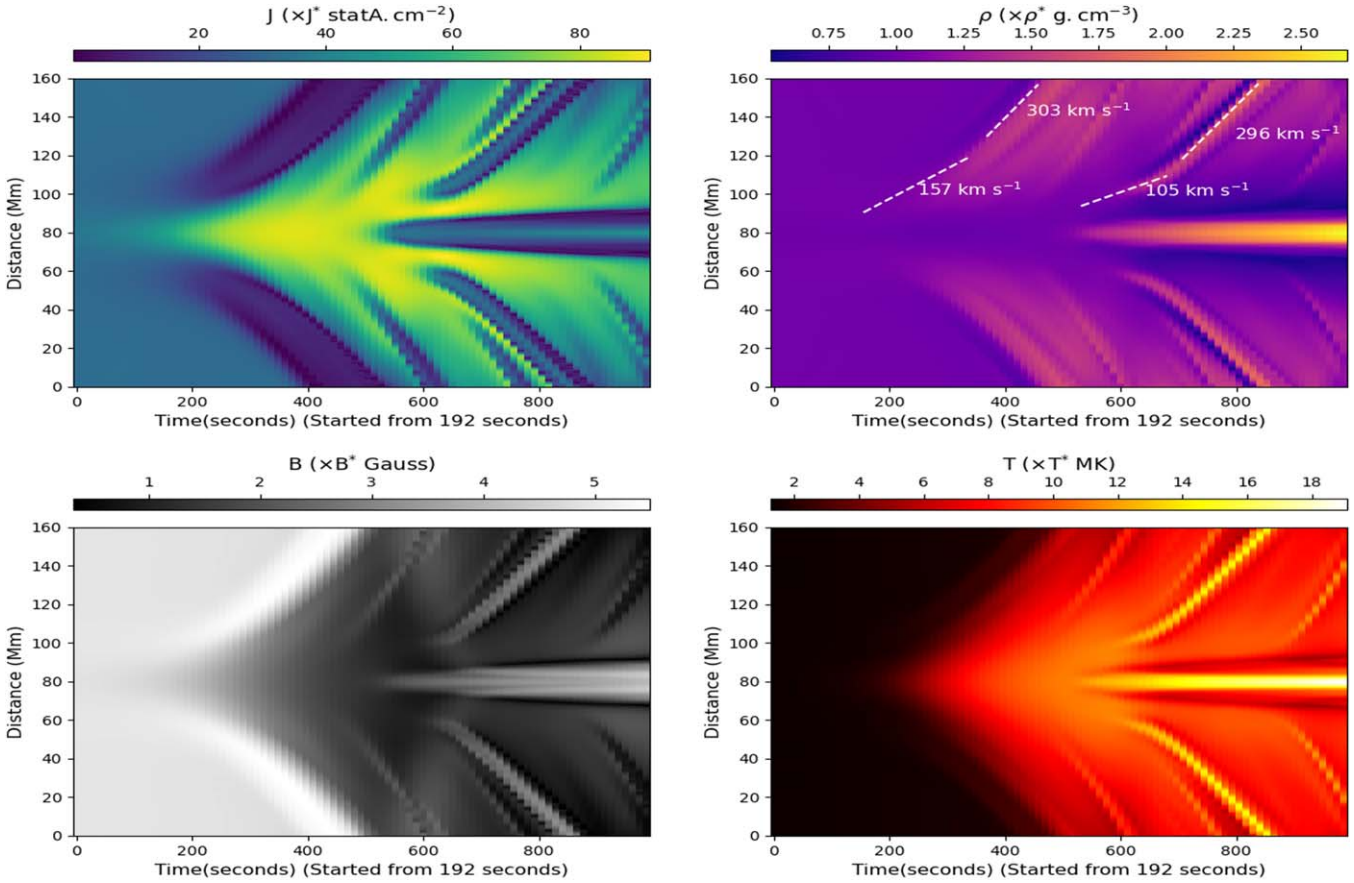

Figure 7. Time–distance maps of J, density, B, and temperature extracted from a slit extended from 20 to 180 Mm along the CS at $x = 0$ Mm. These maps show the temporal evolution of the variables along the CS. They clearly show the bidirectional outflows, three stages of bidirectional movement of plasmoids, and the growth of the steady central plasmoid.

tearing eventually gives rise to the formation of new plasmoids in those regions, as shown in the third and fourth columns of Figure 6. During this stage, two more off-centered plasmoids are formed at larger distances from the center of the CS. Eventually all those off-centered plasmoids move outward with time. Therefore, a third stage of plasmoid formation takes place around 1130 s. These plasmoids also eventually move out along the CS (as shown in the last two columns of Figure 6). The temporal evolution of the CS from the initiation of fragmentation followed by multiple stages of tearing and plasmoid formation is clearly exhibited in the animation accompanying Figure 6. The different stages of plasmoid formation and their outward movements are evident also in the time–distance map of Figure 7. The entire temporal regime for the multiple stages of tearing is shown in the animation of density, J, and temperature. The plasmoids grow during their outward motion. The central plasmoid also grows in time to a larger size than the other plasmoids. It can absorb plasma from up to the midpoint of the CS layer connecting the other plasmoids and resulting in the rapid growth of its size. Therefore the plasmoid that formed at the center of the CS evolves to become a monster plasmoid with a higher growth rate than the off-centered plasmoids (e.g., Uzdensky et al. 2010; Loureiro et al. 2012; Nemati et al. 2017). Bhattacharjee et al. (2009) studied tearing without symmetry and found all the plasmoids were swept along the sheet. It will be interesting in the future to compare with their results when a lack of symmetry about the center of the sheet is allowed in the presence of thermal conduction and radiative cooling.

We have so far discussed how the CS undergoes several stages of evolution and eventually reaches an impulsive bursty stage of dynamics in the form of multiple stages of tearing followed by plasmoid formation. Now let us discuss the magnetic, dynamical, and thermal characteristics of the formed plasmoids in the next section. Since the off-centered plasmoids are moving, it is difficult to extract their detailed properties. But we have a nearly steady plasmoid formed at a height of 100 Mm as a result of the symmetry of our simulation setup. Therefore we find the detailed thermal characteristics of this central plasmoid. Moreover, the moving plasmoids and their kinematical properties are tracked in the distance–time maps shown in Figure 7.

3.2. Characteristics of the Plasmoids

(i) From the top row of the Figure 6, the appearance of plasmoids or magnetic islands with O-points can be seen in the x–y plane. In the case of three dimensions, the addition of the z-component of the magnetic field means that they will be magnetic flux ropes. The off-centered moving plasmoids are growing as they are moving outward, and the steady central plasmoid also grows with time. Initially, the internal structure of the plasmoid is difficult to quantify due to its small size. But as time progresses, the plasmoid shows a clear internal

structuring of J with a magnetic O-point at the center of the plasmoid having a higher value of J than its surroundings.

(ii) From the middle row of Figure 6, it can be seen that the plasmoids have higher densities than their surroundings, which results in their presence as bright blobs. Also, a shock moving with the plasmoids is indicated by drastic changes in the density across the plasmoids along the CS. The interaction of these shocks with the plasmoids might accelerate them to higher speeds during their outward movement.

(iii) The maximum density at the core of the central plasmoid is 2.8 times the background coronal density during its growth. The average density of this plasmoid is estimated to increase up to twice the background coronal density.

(iv) The temperature within the plasmoids is higher than their surroundings. As the plasmoids grow bigger in size, the temperature within them also shows an internal structuring. The magnetic O-point is hotter than the ambient neighborhood within the plasmoid, possibly due to the enhanced ohmic heating there (as shown in the bottom row of Figure 6).

(v) The maximum temperature at the core of the centered plasmoid is 20 MK during its growth, whereas its average temperature is 8 MK.

(vi) We estimate the speed of the outflow as well as the outward moving plasmoids from the time–distance map of density. It can be seen that the outflow speed increases from 157 to 303 km s^{-1} ($0.27v_A$ to $0.52v_A$) during their outward passage (as shown in the density time–distance map in Figure 7). This acceleration of the reconnection outflow might be due to the magnetic tension force.

Along with this continuous outflowing plasma, there exist distinct chunks of plasma in the form of plasmoids which are moving out along the CS. We find that the speed of the plasmoids is also increasing during their passage, from 105 to 296 km s^{-1} ($0.18v_A$ to $0.51v_A$), since they are being accelerated by the magnetic tension force.

4. Discussion

We impose a Gaussian velocity pulse, as a model of fast magnetoacoustic waves, to disturb an elongated CS under solar coronal conditions. The interaction of the pulse with the CS eventually results in a inward pressure as well as a density gradient toward the CS in the x-direction. This gradient results in a bidirectional inflow, which eventually drives magnetic reconnection in a small diffusion layer. This magnetic reconnection initially possesses a Petschek-type character with the presence of slow-mode MHD shocks at the ends of the diffusion layer, as described in Section 3.1.1, and shown in Figure 3 and in the left column of Figure 4. Due to an unbalanced magnetic tension force, a bidirectional outflow sets in to stretch the effective diffusion layer. Eventually, the CS becomes of Sweet–Parker type for a short period. Gradually, tearing or plasmoid instability sets in via the fragmentation of the physical quantities such as current density, magnetic field, and total pressure, as described in Section 3.1.2 and depicted in Figure 5. The plasmoids become properly visible around 733 s of the simulation. Initially, three plasmoids are formed within the CS. Two off-centered plasmoids move outward, while the central one remains stationary due to the symmetry of the imposed velocity disturbance and the initial state. Actually, the y-component of the Lorentz force shows that there are equal and opposite forces acting on the central one, which makes it stationary.

Nevertheless, the outward movement of the other two plasmoids results in further thinning, secondary tearing, and plasmoid formation within the CS. This secondary stage of tearing is followed by two similar stages of plasmoid formation up to the end of the simulation, i.e., 1178 s. Even though the reconnection process finally operates in an impulsive and bursty manner, we note that the proxy of the reconnection rate, i.e., ηJ_{max} (middle panel of Figure 2) undergoes a prominent rapid fall later after the primary onset of tearing. Actually, if a plasmoid grows to a large size but is restricted to remain at the center of the computational domain as in our case due to the imposed symmetries, the plasmoid instability hardly reaches a highly nonlinear phase. Even if it attains that phase it will be short lived and will eventually result in a rapid fall of the reconnection rate (Bhattacharjee et al. 2009). Next, let us make a few remarks about the initial simulation setup and its final outcome in the context of magnetic reconnection in the solar corona.

4.1. Physical Feasibility of the Dynamics

As noted above, we have performed a numerical simulation of magnetic reconnection under solar coronal conditions, i.e., a system with a high Lundquist number subjected to external velocity perturbations. Now, when simulating magnetic reconnection in a high-Lundquist-number system, if the resolution is not very high, one needs to assess whether the dynamics are physically viable. Now for Lundquist numbers 2.51×10^5 and 6.28×10^5, Bhattacharjee et al. (2009) used [2001, 1001] and [3001, 1001] grid points, respectively. Also, Sen & Keppens (2022) have studied plasmoid-related physics with [2048, 2048] grid points with the smallest grid size being 125 km using `MPI-AMRVAC` and the highest value of their Lundquist number is 2.34×10^5. Thus, our value of the Lundquist number, i.e., 4.8×10^5 is about twice their value. So, to find out whether the highest resolution with [2048, 2048] grid points with a smallest grid size of 97.5 km in our work is sufficient or not, we need to examine whether our physical choice of resistivity is higher than the numerical resistivity. Simultaneously, we need to check whether we have more than one grid point within the inner layer of the tearing mode. We find that our model does satisfy these two important criteria, and so it is likely to generate physically acceptable results. These estimates are discussed in detail in Appendix A. In addition, a strong guide field is present in the solar corona and can have significant impact on plasmoid dynamics. Hence we examined whether our choice of magnetic setup provides a nonzero guide field in the vicinity of the CS or not (see the details in Appendix B). It is found that an appropriate guide field is present in the highly localized coronal CSs.

4.2. Comparison with Observations

Here, we compare the dynamics and reconnection in the modeled solar coronal CS with features of CSs and plasmoid dynamics seen in various observations. However, an accurate estimate of plasma beta, guide field, and Alfvén speed is not possible. But we can compare the properties of the plasmoid dynamics qualitatively with those reported in the various solar

coronal observations. Basically we intend to compare the morphological plasma dynamics seen in observations with our CS dynamics. This enables us to infer some physical information regarding the observed CS dynamics. Zhang et al. (2016) estimated the number density of observed plasma blobs in EUV jets to be 1.7–2.8 times the number density of the background solar corona. So, our estimate of the average density of the plasmoids being twice the background density of the solar corona, as well as the maximum density at the core of the plasmoids being 2.8 times the solar coronal plasma density, compare well with the observational estimates. The average temperature of the plasmoids is estimated to be up to 8 MK. Lu et al. (2022) reported an observation of tearing instability in the CS of a solar flare in which they found the blob temperature to be around 6.4 MK initially, which later increased to 7.7 MK. So our estimated average plasmoid temperature is similar to what is measured for plasma blobs in observations. We found the speeds of reconnection outflows to be 157–303 km s^{-1} and of outward moving plasmoids to be 105–296 km s^{-1}. These estimates are very similar to those reported in various coronal observations (Takasao et al. 2012; Zhang et al. 2016). We also noticed that both the reconnection outflows and plasmoids accelerate in time. Bárta et al. (2008) reported similar acceleration characteristics of reconnection outflows and plasmoids. So we see that the dynamical properties of plasmoids as well as their temperature and density are very similar to those seen in coronal observations. We find that the maximum temperature at the core of the central plasmoid reaches up to 20 MK. Also there exists an internal structuring of density and temperature within all the plasmoids. Yokoyama & Shibata (1997) reported that the presence of thermal conduction does not have a significant effect on the reconnection rate and energy release rate. Nevertheless, this high value of the temperature at the core of the plasmoids (due to enhanced ohmic heating there) as well as the internal structuring of density and temperature are likely to be affected when we include thermal conduction and radiative cooling effects in future. In the next subsection, we discuss the inference of the velocity amplitude of the disturbances on CS dynamics.

4.3. Dependence on the Amplitude of the Velocity Pulse

Fast MHD waves or EUV waves can have different strengths in the solar corona. So we have tried different amplitudes for the velocity pulse to find out their effect on the reconnection. Although the physics of the different processes are similar, there are some variations in dynamical behavior as follows:

I. We find that the intermediate time between initiation and end of the CS thinning phase depends on the amplitude of the velocity pulse. For higher amplitudes, this CS thinning phase occurs more quickly.
II. The transformation from Petschek to Sweet–Parker reconnection also happens earlier in time for higher amplitudes of the velocity pulse.
III. The temporal length of the Sweet–Parker regime of reconnection is similar in all the cases and so independent of the amplitude of velocity pulse.
IV. Likewise there is little dependence of the tearing stages on the amplitude of the pulse. Multistage formation and evolution of plasmoids takes place in a self-consistent manner, independent of the amplitude of the pulse.

Besides, a change in the position of the pulse while preserving symmetry is similar to a change in amplitude. Now if the pulse is positioned asymmetrically about the center of the simulation box, it has different effects since the disturbance created in the CS will no longer be symmetric about its length. It will be interesting to examine this asymmetric interaction of the velocity disturbance with the CS independently in a future study. Indeed, a more extensive parametric study with different CS widths in presence of asymmetric pulses can be carried in the future.

5. Conclusions

There are many studies of fast reconnection and plasmoid formation in the literature in which the authors initiate magnetic reconnection by a localized enhancement of resistivity (e.g., Yokoyama & Shibata 1997; Baty et al. 2009; Baty 2012). On the other hand, Odstrcil & Karlicky (1997a) simulated the interaction of a shock wave with a CS, resulting in reconnection via the onset of a tearing-mode instability. Potter et al. (2019) also examined the effect of different forms of periodic external velocity perturbations and the initial configuration of a CS on the dynamics of reconnection and the energy release process. Usually, they used an anomalous resistivity above a current density threshold to achieve fast reconnection and plasmoid formation. Odstrcil & Karlicky (1997a) used pressure perturbations to mimic shock waves. Potter et al. (2019) used periodic perturbations which are present for the entire time of the simulation to drive reconnection.

Both MHD waves and CSs are likely to be ubiquitous in the solar corona. Therefore, EUV waves or fast MHD waves may sometimes in turn trigger reconnection in other regions, especially where prominences are located (Srivastava et al. 2019). Now in the solar corona, eruptions are accompanied by the generation and propagation of EUV waves away from the eruption in a transient manner rather than in a periodic or continuous process (Warmuth 2015; Chen 2017; Cunha-Silva et al. 2018; Liu et al. 2018). In this present paper we mimic such a transient process by a Gaussian velocity pulse at the beginning of the simulation. We consider uniform resistivity instead of a localized enhancement of resistivity or an anomalous resistivity to initiate reconnection. This consideration is of interest in the context of externally driven or forced reconnection in the nonideally conductive solar corona. Therefore we have provided a detailed scenario for the physical processes such as thinning, fragmentation of the CS, and magnetic reconnection when a localized CS is subjected to fast external magnetoacoustic perturbations. In addition, the evolution of various dynamical plasma processes such as flows, plasmoids, shocks, etc., in various phases of the reconnection are also discussed.

This study augments the existing literature on the theoretical baseline of impulsive bursty reconnection through plasmoid instabilities (e.g., Huang & Bhattacharjee 2010, 2012, 2013; Huang et al. 2015; Huang & Bhattacharjee 2016) by (i) exploring the triggering of CS instability by an external driver (specifically, a velocity pulse) in the presence of a uniform resistivity, and (ii) employing plasma parameters relevant to the Sun's corona. Simultaneously, our results are consistent with the latest observations showing the onset of reconnection and associated plasma dynamics by external perturbations in the corona (e.g., Li et al. 2018; Srivastava et al. 2019, 2021). Therefore this study of the different stages of reconnection

which eventually triggers plasmoid formations can be a ready reference to explain observations of reconnection following external forcing via the propagation of transient EUV or fast MHD waves triggered during solar eruptions. Even though this present paper focuses on understanding the dynamics of CSs formed specifically in the solar corona, the present model may be suitably adopted in future to study the details of CS dynamics and magnetic reconnection in other systems.

Acknowledgments

We acknowledge the scientific comments of the reviewer that improved our manuscript considerably. S.M. would like to acknowledge the financial support provided by the Prime Minister's Research Fellowship of India. A.K.S. acknowledges the ISRO grant DS 2B-13012(2)/26/2022-Sec.2 for the support of his scientific research. D.I.P. gratefully acknowledges support through an Australian Research Council Discovery Project (DP210100709). D.Y. is supported by the National Natural Science Foundation of China (NSFC; grant Nos. 12173012, 12111530078, and 11803005), the Guangdong Natural Science Funds for Distinguished Young Scholar (grant No. 2023B1515020049), the Shenzhen Technology Project (grant No. GXWD20201230155427003-20200804151658001) and the Shenzhen Key Laboratory Launching Project (grant No. ZDSYS20210702140800001).

Software: MPI-AMRVAC and Paraview.

Appendix A
Physical versus Numerical Resistivity

Ripperda et al. (2019) reported that their simulation of plasmoid formation within the CS at low resolution is predominantly driven by numerical resistivity rather than imposed physical resistivity. They varied the base resolution and maximum level of refinement for various values of the physical resistivity to find out the effective resolution beyond which the thickness of the CS no longer depended on the resolution, i.e., numerical resistivity does not play any role in the dynamics. Since in our case the maximum resolution is 97.5 km, we make an attempt to find out whether the dynamics are really happening due to physical resistivity or whether they are influenced by numerical resistivity. So, we carry out a comparative study of the thinning phase of the CS for zero physical resistivity. It is expected that if the resistivity is smaller, the diffusion timescale of the CS will be larger. Smaller diffusion results in faster thinning of a CS subjected to an external perturbation. The thinning of the CS is found to be faster in the case of numerical resistivity only, i.e., zero physical resistivity, compared to that for a finite physical resistivity of 2×10^{-4} (shown in the left panel of Figure 8). The increase in the maximum of J also follows the same trend (shown in the middle panel of Figure 8). Similarly, the aspect ratio of the CS also increases faster in the case of numerical resistivity, having a power-law exponent in time of 3.10 in comparison to 2.97 in the case of a physical resistivity of 2×10^{-4} (shown in the right panel of Figure 8). So the thinning process of the CS is slower in the case of a finite physical resistivity. Hence we can infer that the imposed physical resistivity is higher than the numerical resistivity for the resolution used in this simulation. So the dynamics reported in this paper are clearly driven by the physical resistivity of 2×10^{-4} as opposed to numerical resistivity. Even though the internal substructuring within the plasmoids is resolved, the resolution and physical resistivity employed in this work preclude the appearance of some smaller-scale dynamics. This is expected to include, for example, the formation of small-scale plasmoids and their coalescence with larger plasmoids.

To justify our chosen value of the imposed resitivity further, we calculate the diffusion layer width (i.e., the width in which the diffusion is really important) to determine whether the inner layer of the tearing mode is fully resolved. We use ϵl as an estimate of the diffusion layer width with ϵ being calculated as $R_m^{-1/4}$ (Priest 2014). The magnetic Reynolds number (R_m) is measured to be of the order of 10^4 using the initial CS width, i.e., 3 Mm, the initial v_A, and the imposed uniform physical resistivity. So we find that diffusion layer width is around 325 km. Since the maximum resolution in this present work is 97.5 km, we infer that there is are at least three grid points within the inner layer of tearing. Therefore the resolution of the simulation is capable of resolving the diffusion layer connected to the tearing mode.

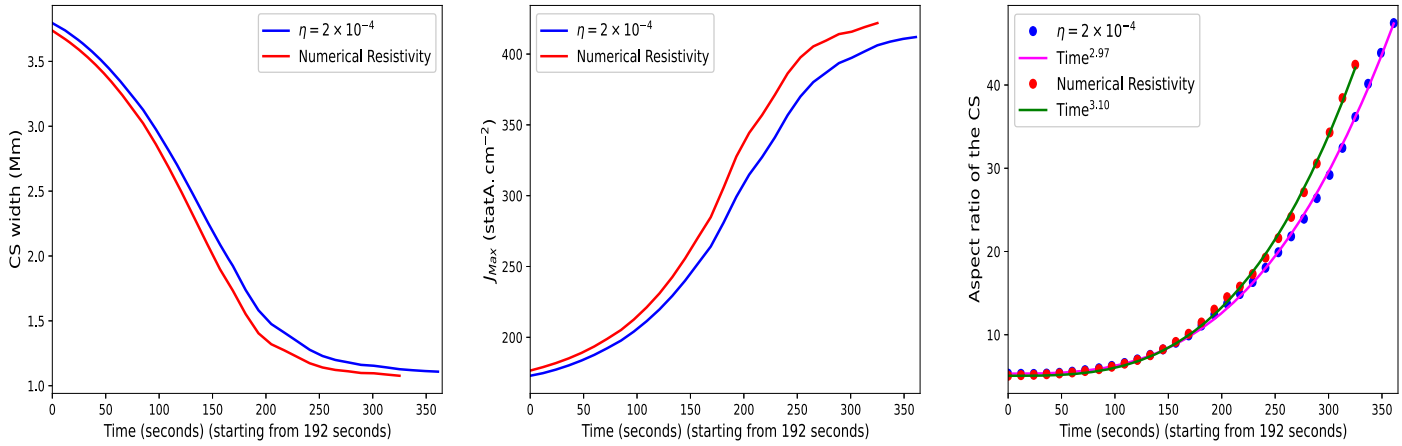

Figure 8. Left: temporal evolution of the CS width at a height of 100 Mm for imposed physical resistivity (blue curve) and numerical resistivity (red curve). Middle: temporal evolution of the maximum J for imposed physical resistivity (blue curve) and numerical resistivity (red curve). Right: temporal evolution of the aspect ratio of the CS for imposed physical resistivity (blue curve) and numerical resistivity (red curve). It is evident that the exponent of the power-law fit to the curves of the aspect ratios changes from 2.97 to 3.10 when we omit the physical resistivity.

Appendix B
Relevance of the Initial Magnetic Field Configurations

We are simulating externally driven or forced magnetic reconnection and the associated dynamics in solar coronal conditions. So we must ensure that the numerical setup is initially in magnetohydrostatic equilibrium before giving any external perturbations like a velocity pulse in our case. We had two choices to establish an equilibrium initial state as follows:

I. We may adopt the field of a normal simple CS with, say, a tanh profile for $b_y(x)$, balanced by the plasma pressure $p(x)$ without or with a uniform guide field b_z.
II. We may consider the same profile for $b_y(x)$ balanced by a force-free guide field $b_z(x)$ with the pressure, density, and magnetic field being uniform.

Since in practice there is usually a strong guide field present in the corona, we decided to adopt a force-free CS with uniform plasma pressure instead of a magnetostatic CS with a strong central plasma pressure. Importantly, this incorporates the effect of a guide field inside the central part of the CS and extending quite some distance outside it. It is worth mentioning that the half-width of the CS is 1.5 Mm whereas the guide field tends to zero at more than 5 Mm from the center of the CS, as shown in the right panel of Figure 9. Therefore a nonzero guide field is present in the nearest vicinity of the CS in which all the dynamics are occurring. Hence it ensures the "force freeness" of the initial system for homogeneous and isotropic plasma parameters in the solar corona. A stronger guide field than considered here may be more relevant to many solar flares, and its inclusion can be carried out as a separate study in the future.

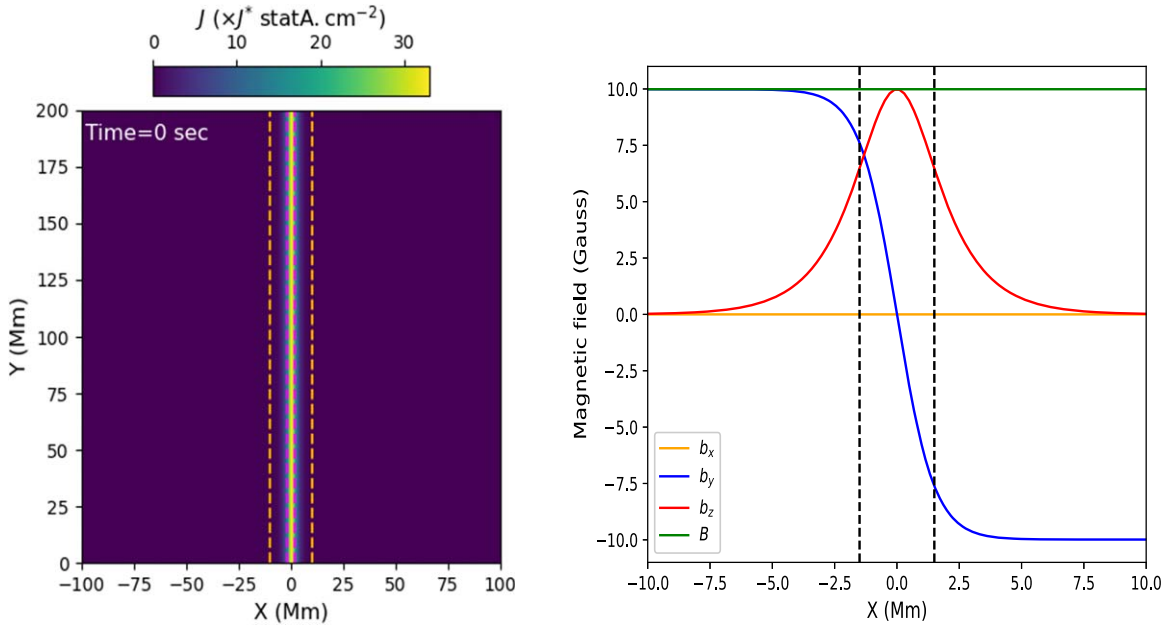

Figure 9. Left: map of the current density (J), showing the CS as a region of higher J whose extents are bounded by magenta dashed lines. The region within the pair of orange dashed lines is taken under consideration to show the profile of the magnetic field magnitude and its components. Right: profiles of the magnetic field components. The red curve gives the profile of the guide field, which shows that the guide field vanishes at a distance of more than 5 Mm from the center of the CS. The pair of black dashed vertical lines denote the extent of the CS, which has a half-width of 1.5 Mm.

Appendix C
Reason behind the Steady Behavior of the Centered Plasmoid

For the present case, the initial magnetic field does not possess any complex asymmetrical geometry. In addition, the initial pulse that we imposed is symmetrical in the y-direction. It originates from $y = 100$ Mm with an isotropic standard deviation (SD), i.e., direction independent SD. The magnetic field lines are purely vertically directed without any curvature or discontinuity except at the CS itself. Therefore, the pulse interacts with the CS in a symmetrical manner about the midpoint at $y = 100$ Mm. Now the dynamics of the plasmoids—i.e., whether it will move or remain steady—will depend upon the resultant force acting on it. So we investigate the y-component of the Lorentz force during different stages of plasmoid dynamics, as exhibited in Figure 10 and its animated version.

From Figure 10, it can be noticed that in the cases of plasmoids moving along the CS, the y-component of the Lorentz force just above and below the plasmoids has the same orientation, i.e., in the outward direction. On the contrary, the y-component of Lorentz force has a much lower magnitude in close proximity to the centered plasmoid. Besides, those are directed in opposite directions at the opposite extents of the centered plasmoid. Hence the net resultant force on the centered plasmoid is almost zero or relatively negligible, keeping it steady at the middle of the CS during its growth with time. So it is the initial symmetric magnetic configuration without any curvature that leads to the isotropic propagation of the initial velocity pulse before its interaction with the CS, which results in this steady growth of the centered plasmoid. However, it should be noted that in some previous numerical models, by imposing random perturbations the central monster plasmoid does not form (e.g., Huang & Bhattacharjee 2010, 2012, 2013; Huang et al. 2015; Huang & Bhattacharjee 2016). It will be a matter of future investigation regarding how the plasmoids will form under an initial perturbation that is not completely symmetric, and when nonideal plasma conditions are switched on.

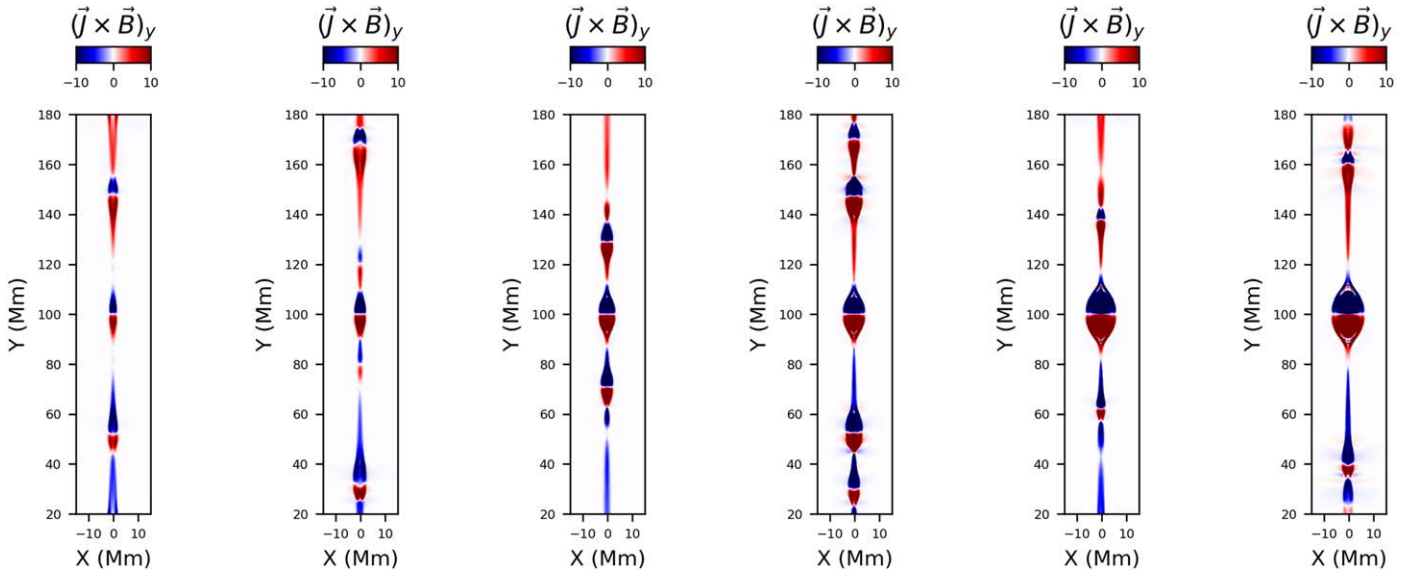

Figure 10. Snapshots of the y-component of the Lorentz force $(\boldsymbol{J}\times\boldsymbol{B})_y$ at times 733, 781, 866, 938, 1130, and 1178 s of the resistive MHD simulation. It is evident that $(\boldsymbol{J}\times\boldsymbol{B})_y$ has the same direction above and below the off-centered plasmoids, which drives the plasmoids out. But the direction of $(\boldsymbol{J}\times\boldsymbol{B})_y$ just above and below the central plasmoid is oppositely directed, giving no resultant net force. The entire evolution of this quantity from 601 to 1178 s is available as an animation. The real-time animation duration is 5 s. The green rectangular box used in the animation shows the field of view exhibited in this figure.

(An animation of this figure is available.)

References

Asai, A., Ishii, T. T., & Kurokawa, H. 2001, ApJL, 555, L65
Bárta, M., Vršnak, B., & Karlický, M. 2008, A&A, 477, 649
Baty, H. 2012, PhPl, 19, 092110
Baty, H., Priest, E. R., & Forbes, T. G. 2009, PhPl, 16, 060701
Bhattacharjee, A., Huang, Y. M., Yang, H., et al. 2009, PhPl, 16, 112102
Birn, J., & Priest, E. R. 2007, in Reconnection of Magnetic Fields: Magnetohydrodynamics and Collisionless Theory and Observations, ed. J. Birn & E. R. Priest (Cambridge: Cambridge Univ. Press)
Biskamp, D. 2000, Magnetic Reconnection in Plasmas (Cambridge: Cambridge Univ. Press)
Chen, J., Erdélyi, R., Liu, J., et al. 2022, FrASS, 8, 238
Chen, P. 2017, SCPMA, 60, 29631
Cheng, X., Li, Y., Wan, L. F., et al. 2018, ApJ, 866, 64
Cowling, T. G. 1953, in The Sun, ed. G. P. Kuiper (Chicago, IL: Univ. Chicago Press), 532
Cunha-Silva, R. D., Selhorst, C. L., Fernandes, F. C. R., et al. 2018, A&A, 612, A100
Fárník, F., Kaastra, J., Kálmán, B., et al. 1983, SoPh, 89, 355
French, R. J., Matthews, S. A., van Driel-Gesztelyi, L., et al. 2020, ApJ, 900, 192
Furth, H. P. 1963, PhFl, 6, 48
Huang, Y. M., & Bhattacharjee, A. 2010, PhPl, 17, 062104
Huang, Y. M., & Bhattacharjee, A. 2012, PhRvL, 109, 265002
Huang, Y. M., & Bhattacharjee, A. 2013, PhPl, 20, 055702
Huang, Y. M., & Bhattacharjee, A. 2016, ApJ, 818, 20
Huang, Y. M., Bhattacharjee, A., Guo, L., et al. 2015, Solar Heliospheric and Interplanetary Environment Conf. (SHINE 2016), 26
Keppens, R., Meliani, Z., van Marle, A. J., et al. 2012, JCoPh, 231, 718
Li, L., Zhang, J., Peter, H., et al. 2018, ApJL, 868, L33
Liu, W., Jin, M., Downs, C., et al. 2018, ApJL, 864, L24
Liu, Y., Luhmann, J. G., Lin, R. P., et al. 2009, ApJL, 698, L51
Longcope, D., Unverferth, J., Klein, C., et al. 2018, ApJ, 868, 148
Loureiro, N. F., Samtaney, R., Schekochihin, A. A., et al. 2012, PhPl, 19, 042303
Loureiro, N. F., & Uzdensky, D. A. 2016, PPCF, 58, 014021
Lu, L., Feng, L., Warmuth, A., et al. 2022, ApJL, 924, L7
Nemati, M. J., Wang, Z. X., & Wei, L. 2017, ApJ, 835, 191
Norman, C. A., & Smith, R. A. 1978, A&A, 68, 145
Odstrcil, D., & Karlicky, M. 1997a, A&A, 326, 1252
Odstrcil, D., & Karlicky, M. 1997b, AdSpR, 19, 1895
Ofman, L., & Liu, W. 2018, ApJ, 860, 54
Pontin, D. I., & Priest, E. R. 2022, LRSP, 19, 1
Porth, O., Xia, C., Hendrix, T., et al. 2014, ApJS, 214, 4
Potter, M. A., Browning, P. K., & Gordovskyy, M. 2019, A&A, 623, A15
Priest, E. 2014, in Magnetohydrodynamics of the Sun, ed. E. Priest (Cambridge: Cambridge Univ. Press)
Priest, E. R., & Forbes, T. G. 1986, JGR, 91, 5579
Ripperda, B., Porth, O., Sironi, L., et al. 2019, MNRAS, 485, 299
Sakai, J. I. 1983, JPlPh, 30, 109
Sakai, J. I., & Washimi, H. 1982, ApJ, 258, 823
Sen, S., & Keppens, R. 2022, A&A, 666, A28
Shen, C., Chen, B., Reeves, K. K., et al. 2022, NatAs, 6, 317
Srivastava, A. K., Mishra, S. K., Jelínek, P., et al. 2019, ApJ, 887, 137
Srivastava, A. K., Mishra, S. K., & Jelínek, P. 2021, ApJ, 920, 18
Svestka, Z. 1981, Solar Flare Magnetohydrodynamics (New York: Gordon and Breach), 47
Takasao, S., Asai, A., Isobe, H., et al. 2012, ApJL, 745, L6
Treumann, R. A., & Baumjohann, W. 2015, A&ARv, 23, 4
Uzdensky, D. A. 2011, SSRv, 160, 45
Uzdensky, D. A., Loureiro, N. F., & Schekochihin, A. A. 2010, PhRvL, 105, 235002
van der Holst, B., Keppens, R., Meliani, Z., et al. 2012, MPI-AMRVAC: MPI-Adaptive Mesh Refinement-Versatile Advection Code, Astrophysics Source Code Library, ascl:1208.014
Wang, H., Chae, J., Yurchyshyn, V., et al. 2001, ApJ, 559, 1171
Warmuth, A. 2015, LRSP, 12, 3
Xia, C., Teunissen, J., El Mellah, I., et al. 2018, ApJS, 234, 30
Yamada, M., Yoo, J., & Myers, C. E. 2016, PhPl, 23, 055402
Yan, X., Xue, Z., Jiang, C., et al. 2022, NatCo, 13, 640
Yokoyama, T., & Shibata, K. 1997, ApJL, 474, L61
Zhang, Q. M., & Ji, H. S. 2014, A&A, 561, A134
Zhang, Q. M., Ji, H. S., & Su, Y. N. 2016, SoPh, 291, 859
Zheng, R., Chen, Y., Feng, S., et al. 2018, ApJL, 858, L1
Zheng, R., Jiang, Y., Yang, J., et al. 2014, MNRAS, 444, 1119
Zheng, R., Wang, B., Zhang, L., et al. 2022, ApJL, 929, L4
Zhou, G., Gao, G., Wang, J., et al. 2020, ApJ, 905, 150
Zweibel, E. G., & Yamada, M. 2009, ARA&A, 47, 291